# On the coupled integration of ducted heat-exchanger systems for aviation

Erik Hasselwander<sup>1</sup>, Isak Jonsson<sup>1</sup>, Anders Lundbladh<sup>2</sup>, Petter Miltén<sup>1</sup>, and Carlos Xisto<sup>1</sup>

<sup>1</sup>Chalmers University of Technology, Mechanical and Maritime Sciences, Gothenburg, Sweden

E-mail:, erikhass@chalmers.se

<sup>2</sup>GKN Aerospace Sweden AB, Trollhättan, Sweden

## **Abstract**

This paper investigates the design and aerothermal optimization of duct geometries with integrated finned heat exchangers. The primary focus of the paper is to investigate how the performance varies with heat exchanger inlet area and total duct length. The results provide new insights into the underlying trade-offs. Heat exchangers with a larger area result in lower losses over the heat exchanger matrix but incur increased losses in the ducts. Additionally, shorter ducts lead to higher losses over the heat exchanger due to the reduced diffusive capacity, while duct losses remain largely unchanged. The study also investigates the effects of the matrix configuration in the heat exchanger overall aerodynamic performance. A fixed and optimized geometry is therefore selected and the impact of decreased flow restriction in the heat-exchanger transversal direction is investigated. The results show that removing the fins, leads to a negligible increase in the normalized losses from 1.146 to 1.159, indicating that the pressure drop across the heat exchanger matrix is the primary driver of diffusion, rather than by the finned structure itself.

Keywords: Aviation, aerodynamics, heat-exchanger, CFD

# 1 Introduction

The transition to hydrogen-fueled aviation presents significant challenges in thermal management, particularly in the integration of high-performance, compact heat exchangers. As aviation aims for a 75% reduction in CO<sub>2</sub> emissions by 2050 [1], hydrogen-powered gas turbine engines are a promising solution. Future civil and military engines will face increased thermal loads, necessitating the integration of megawatt-class heat exchangers while maintaining aerodynamic efficiency. When integrated into an aircraft engine, compact heat exchangers are favoured to minimize drag and weight penalties, which are critical factors in aviation design. This leads to challenging configurations that require short diffuser ducts coupled with flow turning that are more prone to flow separation and increase in pressure losses. Finding a good compromise between integration and performance has been the focus of several ongoing and earlier attempts. A key issue is that HEX integration has remained very much casespecific and ad-hoc oriented. There is a lack of a structured design approach, which typically makes HEX integration time-consuming and often leads to suboptimal configurations. Despite decades of research, there is still no widely accepted methodology that allows engineers to confidently integrate HEX into propulsion systems without relying in case studies.

One example of a coupled HEX-diffuser installation is shown in Figure 1. The engine represents a hydrogen-fuelled turbofan, where cryogenic hydrogen is used to cool down the inter-compression air via an intercooler-HEX. However, a similar design could be used with kerosene or SAF, cooling the flow with bypass air or to use the compressor air to cool a cooling fluid for aircraft systems. In the same figure different solutions are proposed to both reduce the installation size and losses. If the diffusing duct is short, there is a risk of flow separation which reduces the pressure and gives a slow flow in part of the HEX, which reduces cooling as seen in configuration 1. For a more compact design, turning vanes can be added as shown in configuration 2. The purpose of these vanes is to control the turning while diffusing the flow, similar to stator vanes in a compressor. Such configuration can be complemented with bleed ducts, possibly with actively controlled valves (configuration 3), either for further compactness or for stable operation in off-design.

The main objective of this paper is to advance the development of a computational design tool for the design generation diffuser ducts with embedded heat exchangers. A key aspect of this development is the incorporation of a generalized heat exchanger model capable of accurately representing aerothermal performance within a continuum-based mod-

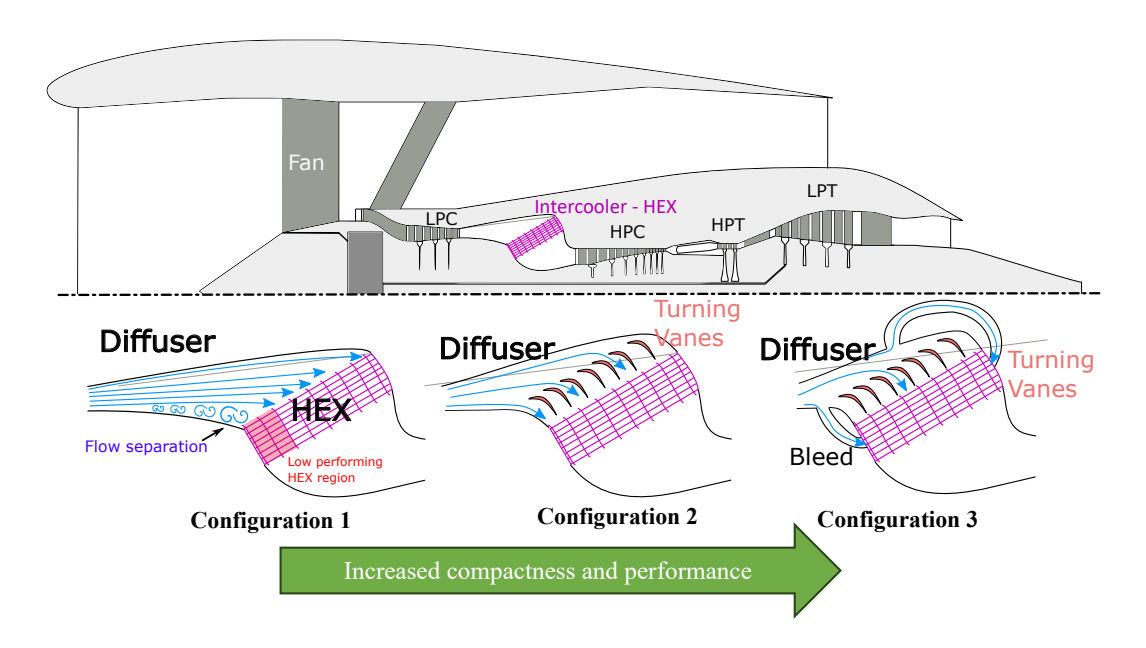


Figure 1: Example on how to achieve a compact heat-exchanger integration by applying different technologies. The complexity added from left to right is expected to allow for trades between installation size and losses. Some technologies will also be able to increase the flow stability in the most demanding off-design conditions. LPC-Low-pressure compressor; HPC – high-pressure turbine, LPT – Low-pressure turbine.

eling framework. In addition, the paper seeks to present a conceptual design suitable for implementation and validation within the Chalmers low-pressure compressor rig test facility, thereby contributing to the first steps towards verification of the proposed modeling approach. A number of optimized configurations were investigated for varying diffuser area ratio and total duct length. The results provide new insights into the underlying design trade-offs while accounting for thermal and aerodynamic performance. In the present study the impact of flow stability was not considered.

# 2 Methodology

This section describes the methodology used to design intermediate compressor ducts with integrated heat exchangers. The duct was designed for integration in the Chalmers 2.5 stage low-pressure compressor test rig which put forth several design constraints. This is expressed through geometric and flow boundary conditions as well as the use of water as the coolant internal fluid. The overall geometry considered is shown in Figure 2, and comprises a diffusing duct, a contracting duct, and the heat exchanger.

The inlet corner points are constrained by the outlet duct geometry of the Chalmers 2.5-stage compressor test rig. As the test rig consists of only a single compressor, and thus has nothing downstream of the duct, there were no fixed outlet corner points or duct length constraints imposed by the existing setup. The outlet corner points were chosen to maintain the same cross-sectional area as the inlet, while reducing the mean radius. The mean radius was reduced by  $R_{inlet} - R_{outlet} = \Delta R = 0.2 \,\mathrm{m}$ , which is a typical value for engines of this size. The heat exchanger length was set to  $L_x = 0.09 \,\mathrm{m}$ , consistent with the configuration used in [2, 3].

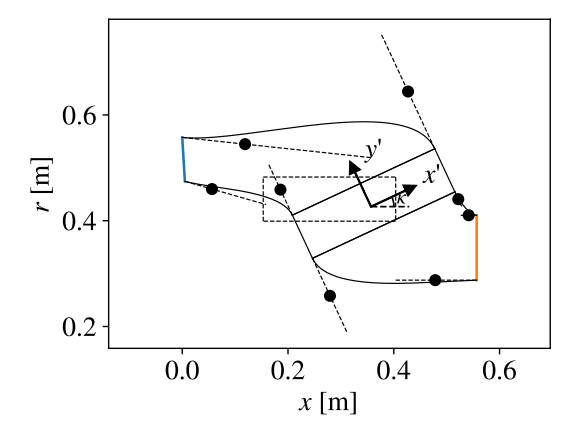


Figure 2: Meridional view of an intermediate compressor duct with an integrated heat exchanger. The blue lines represents the respective domain inlets and the orange lines represent the outlets. The figure also shows the Bezier control points used to parametrize the geometry.

The overall duct length was determined using the engine duct parameter  $\Delta R/L$ , defined as the ratio between the change in mean radius from inlet to outlet and the total length of the duct. Aggressive designs typically exhibit values above 0.6, while more conventional designs fall around 0.5 or below. In this study, a baseline value of  $\Delta R/L=0.3$  was selected to achieve a conservative duct design capable of accommodating the heat exchanger within the duct.

## 2.1 Geometry parameterization

The geometry is parameterized through 11 variables that relate to the heat exchanger and duct geometries. The paramet-

ers are illustrated in the geometry in Figure 2. Three parameters,  $x_{hex}$ ,  $y_{hex}$  and  $\kappa$ , control the location and angle of the heat exchanger. The remaining eight parameters,  $\lambda_1$  through  $\lambda_8$ , control the position of the control points for the splines that define the duct walls. Figure 2 shows the bounds of the control points as the dashed lines, the dots are the position of the control points for  $\lambda_n = 0.25$  and the dashed square in the center is the bounding box for the midpoint of the heat exchanger. The black points, as well as the start and end points of the curve are used to parameterize the geometry. The length of the dashed lines are a fraction of the length between the corner points of the curves, determined by  $\lambda$ . The angle of the dashed lines are tangential to the connecting curves as this ensures a smooth transition between the curves. Thus the resulting splines have two degrees of freedom each which restricts the possible geometries.

In order to account for the orientation of the heat exchanger within the system, a rotated coordinate system, denoted as the x'-y' coordinate system, is introduced. This local coordinate system aligns with the geometric orientation of the heat exchanger and is defined by a rotation of an angle  $\kappa$  relative to the global x-r coordinate system. The transformation between the global and rotated coordinate systems is expressed as

$$\begin{bmatrix} x' \\ y' \end{bmatrix} = \begin{bmatrix} \cos \kappa & \sin \kappa \\ -\sin \kappa & \cos \kappa \end{bmatrix} \begin{bmatrix} x \\ r \end{bmatrix}. \tag{1}$$

### 2.2 Post processing definitions

To be able to distinguish between different types of losses the duct and heat exchanger is split into four zones: diffusing duct, HEX entry, HEX core and contracting duct. The zone boundaries are defined as in Figure 3. The diffusing duct losses are calculated between line 1 and 2, HEX entry losses are calculated between line 2 and 3, HEX core losses are calculated between line 3 and 4, and the contracting duct losses between line 3 and 4. Line 2 is located upstream of the ICD-HEX interface and line 3 is located downstream of the ICD-HEX interface. The lines are positioned 5 % of the HEX total length in either direction of the interface.

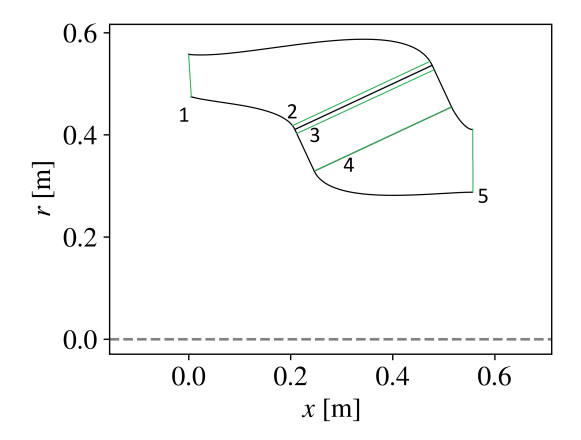


Figure 3: The boundaries, in green, used to distinguish between different sources of losses.

The non-uniformity of the velocity normal to the heat exchanger inlet (the y'-direction), denoted  $\varphi$ , is calculated as

$$\varphi = \frac{\sum_{f} |u_{y',f} - \bar{u}_{y'}| A_f}{2|\bar{u}_{y'}| \sum_{f} A_f}$$
 (2)

where  $\sum_f$  represents the sum over all face,  $\bar{u}_{y'}$  is the surface average of  $u_{y'}$ ,  $u_{y',f}$  denotes the velocity at the face and  $A_f$  is the area of a face. The non-uniformity is a measure used to estimate the degree of diffusion that is achieved at the heat exchanger inlet. For a uniform distribution of velocities the non-uniformity has a value of 0, which increases as the distribution becomes less uniform.

## 2.3 Heat exchanger model

A reference heat exchanger is used to obtain the generalized geometrical parameters needed to calculate the aerothermal performance. The geometrical parameters of the cold side of the reference heat exchanger are kept constant, while the hot side is allowed to vary in order to match a target temperature drop (detailed in Section 2.4.1). The reference heat exchanger used in this paper is the 9.1-0.737-S finned flat-tube type, illustrated in Figure 4. The cold side of the heat exchanger consists of flat tubes while the hot side consists of fins. When matching a target temperature drop the spacing of the fins is varied by changing  $\chi$ .

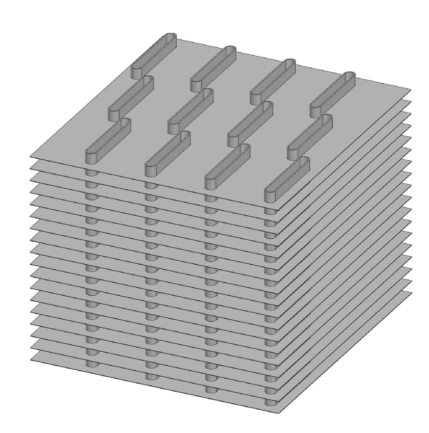


Figure 4: 3D-view of the 9.1-0.737-S heat exchanger geometry. Figure from [2].

Due to the unavailability of hydrogen in the experimental setup, water is employed as the coolant fluid. While cryogenic hydrogen is the intended coolant for hydrogen aircraft, water serves as a practical and accessible substitute suitable for experimental purposes. It is noted that the primary focus of this work is the air-side integration of the HEX, which is also the limiting side when concerning heat transfer performance. Hence, the selection of the coolant is not expected to significantly affect the outcome and conclusions of the following work. The heat exchanger is oriented such that the normal vector of the fins aligns with the x'-axis. The HEX geometrical parameters are obtained from [4] and represented into the geometrical generalization parameters (GGPs) proposed by [5] in Table 1. As mentioned above, the coolant side geometry is retained, hence  $\sigma_c$  (coolant side ratio between passage area and frontal area) and  $\alpha_c$  (coolant side ratio between

*Table 1: Geometrical generalization parameters for the 9.1-0.737-S heat exchanger.* 

Symbol	Value				
Constant					
$\sigma_c$	0.01				
$lpha_c$	160/m				
Initial	Initial values				
χ	0.231				
$lpha_h$	2151/m				
$\alpha_r$	13.45				
$\sigma_h$	0.7589				
$\sigma_r$	75.89				

wetted area and volume) are constant throughout the analysis. In order to match the targeted thermal load, the air-side parameters,  $\sigma_h$  and  $\alpha_h$  are allow to vary with  $\chi$  (solid volume fraction). For more details about how the different geometrical parameters are derived see [6].

The discretized heat exchanger model is implemented in STAR-CCM+ 2410 by treating each individual cell as a small heat exchanger. In each cell the overall heat transfer coefficient and pressure drop terms are calculated according to:

$$\frac{1}{U_h} = \frac{1}{\eta_{o,h}h_h} + \frac{\alpha_r}{\eta_{o,c}h_c} + \frac{2t}{\left(1 + \frac{1}{\alpha_r}\right)k} \tag{3}$$

and

$$\Delta p_0 = \frac{\dot{m}^2}{2\rho_{in}A_{fr}^2} \left( \left( \frac{1}{\sigma^2} + 1 \right) \left( \frac{\rho_{in}}{\rho_{out}} - 1 \right) + 2fL \frac{\alpha}{\sigma^3} \frac{\rho_{in}}{\rho_m} \right) \tag{4}$$

where the heat transfer coefficient for both the air and water side is calculated using:

$$h = \frac{k\alpha \text{Nu}}{4\sigma} = \frac{k\alpha j \text{RePr}^{1/3}}{4\sigma}$$
 (5)

and the following correlations are used to calculate the Colburn and friction factors for both the cold (water) and hot (air) sides,

$$j = 0.360 \left(\frac{\ell}{D_h}\right)^{-0.401} \text{Re}^{-0.413} + 2.13 \times 10^{-5} \left(\frac{\ell}{D_h}\right) \quad (6)$$

and

$$f = 0.492 \left(\frac{\ell}{D_h}\right)^{-0.501} \text{Re}^{-0.232} \tag{7}$$

The Reynolds number for each side of the heat exchanger is calculated using:

$$Re = \frac{4\rho u\sigma}{\alpha u} \tag{8}$$

The heat transfer rate, equation 12, is integrated and divided by the cell volume to obtain the volumetric heat transfer rate  $q_h/V$ ,

$$\frac{q}{V} = U\alpha \left(T_c - T_h\right),\tag{9}$$

The calculated volumetric heat transfer rate is then added as a volumetric source term to the energy equation in the air region, and as a sink term of the same magnitude to the water region. Since the CFD-computed velocity  $u^*$  does not account for the reduced flow area caused by the heat exchanger structure, it is corrected to obtain the actual velocity in the heat exchanger as

$$u = \frac{u^*}{\sigma}. (10)$$

The calculated volumetric heat transfer rate is then applied as a source term in the energy equation for the air region and as a sink term of equal magnitude in the water region.

By assuming that the local variations of density is small, which is valid for a sufficiently fine mesh, we obtain that  $\rho_{in} = \rho_{out} = \rho_m$  which allows us to rewrite equation 4 as

$$\frac{\Delta p_0}{u^2 L} = \frac{\alpha \rho f}{2\sigma^3} \tag{11}$$

as  $\dot{m} = \rho u A_{fr}$ . The pressure loss term is normalized by  $u^2 L$ , where u is the velocity in the local cell, to be applied as a pressure loss term in the x' and y' directions through STAR-CCM+'s porous region inertial resistance. The fins in the heat exchanger do not allow flow in the x' direction. This is captured by increasing the pressure drop in the fin-normal direction, x', by a factor 1000 [2]. For the case study of an isotropic heat exchanger the pressure loss term is set according to Equation 4 in both directions.

### 2.4 CFD modeling

The simulations are carried out using the commercial finite volume code STAR-CCM+ 2410 using a two dimensional, axisymmetric and steady state framework. Two flow fields are solved simultaneously: the air side of the duct, which include the ducts and heat exchanger, and the water side, which includes only the heat exchanger portion of the geometry.

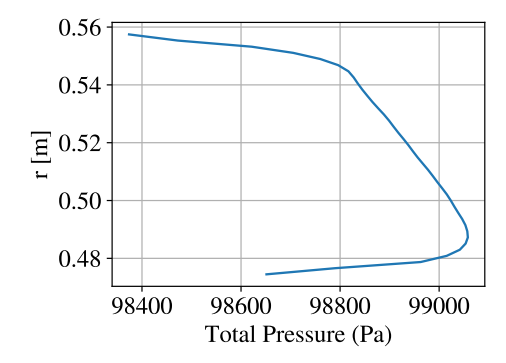
The air side is modeled as a dry compressible ideal gas. The governing equations are the compressible RANS coupled with the  $k-\omega$  SST turbulence model and the energy equation. These equations are solved using a coupled solver with second-order numerical schemes. The temperature dependency of the viscosity is modeled using Sutherland's law. An ideal gas model was employed, even though the Mach number in this study is below 0.3 as the purpose of this work is to validate the model for use in engine conditions where the Mach number is typically in the range of 0.4-0.6.

The air-side inlet boundary conditions are specified using a total pressure profile, a total temperature profile, and a velocity direction specification. The profiles are obtained from a previous three-dimensional RANS simulation that was validated against experimental results [7]. The outlet boundary condition is specified as a uniform pressure outlet which is dynamically adjusted each iteration to match the target mass flow rate. The profiles used are shown in Figure 5 and the related averaged flow properties and relevant physical quantities are shown in Table 2.

The water side of the heat exchanger is modeled as a laminar counterflow configuration with slip wall boundary conditions.

Table 2: Summary of inlet boundary conditions.

Parameter	Value
Total temperature, $T_0$	291.73 K
Total pressure, $p_0$	98 907 Pa
Reynolds number, Re	366 262
Mach number, Ma	0.129
Velocity, v	44.13  m/s
Blockage ratio, $B_T$	24 %



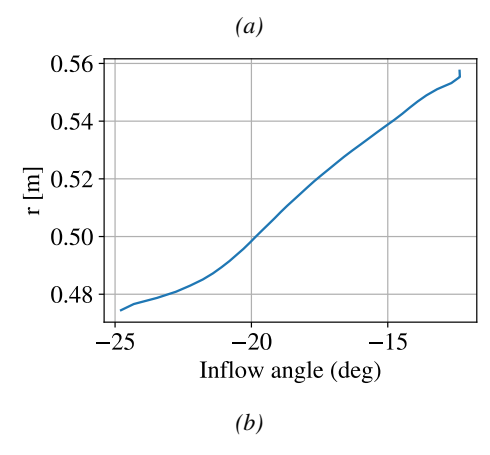


Figure 5: Inlet profiles to the ICD. The figure shows total pressure (a), total temperature (b) and inflow angle (c). The inflow angle is measured against the axial axis.

In this configuration, the coolant flows in the direction opposite to that of the air. This approach attempts to model a cross-flow heat-exchanger with a large number of passes that can be represented as a counter-flow. It should be noted that the water side modeling is only required to establish the coolant flow temperature profile and mass-flow to compute the associated heat-flux using

$$\frac{dq}{dA} = U(T_h - T_c) \tag{12}$$

The overall heat transfer coefficient, U, is computed using the aerothermal model available in GenHEX. At the coolant side inlet, a uniform mass flow inlet with a mass flow rate of  $3 \, \text{kg/s}$  and a temperature of  $278.15 \, \text{K}$  (5 °C) is specified. Heat transfer is modeled as an energy sink term, equal in magnitude and opposite in sign to the energy source term applied on the air side.

### 2.4.1 Matching a target temperature drop

To be able to compare the designs in the optimization loop the thermal load of the heat exchanger was kept constant. This was achieved by numerically changing the spacing of the fins in the heat exchanger until a target temperature drop between the inlet and outlet is reached. To numerically change the spacing the value of  $\chi$  is updated every iteration. Increasing or decreasing  $\chi$  changes  $\sigma_h$  and  $\alpha_h$ , which will impact in the wetted area of the air-side of the heat-exchanger, causing the heat transfer and pressure drops to change. After each iteration of the flow solver a new value of  $\chi$  is calculated as

$$\chi = \chi_{\text{old}} \left( 1 + \psi \frac{\left| \Delta T_{current} - \Delta T_{\text{target}} \right|}{\Delta T_{\text{target}}} \right)$$
 (13)

where  $T_i$  is the current temperature drop,  $T_{target}$  is the target temperature drop,  $\psi$  is an under relaxation factor which is used to tune the convergence.

#### 2.4.2 Numerical mesh

The mesh is a polyhedral mesh with prism layers close to the wall. To ensure that the mesh is sufficiently fine close to the wall for ensuring a  $y^+ < 1$ . The bulk of the mesh was generated using a polygonal mesher.

## 2.5 Solution procedure

The simulations were converged in two steps. The first 400 iterations were run without updating  $\chi$  to allow the flow field to stabilize. Thereafter,  $\chi$  is allowed to change until the desired thermal load is reached. The simulation is terminated when all the residuals have reduced by a factor of  $1 \times 10^6$ . If the simulation has not converged after a total of 1500 iterations the simulation is stopped as the residuals were observed to have stabilized after this. The simulations were discarded if the residuals are reduced by less than a factor  $1 \times 10^3$ .

## 2.6 Optimization

The designs are developed using a single-objective, multivariate Bayesian optimization framework based on the BO\_GP code[8]. The optimization loop consists of six steps:

- 1. Generate geometry inputs using the Bayesian optimization model based on the existing data.
- 2. Generating the duct geometry from the geometry inputs.
- 3. Create a computational mesh.
- 4. Solve for the flow field.
- 5. Post-process the results to extract the target quantity.
- 6. Add the target quantity to the database.

The loop is then repeated until the optimization is considered sufficiently converged. The optimization is used to sweep the area ratio of the heat exchanger for a constant duct length, and the duct length for a constant area ratio. The swept points are shown in Table 3.

In each optimization case the area ratio and length of the duct was fixed. This left the position of the heat exchanger, the inclination of the heat exchanger and the eight Bezier control points to be optimized. The optimization parameters and their

Table 3: Swept area ratio (AR) and corresponding normalized duct length changes ( $\Delta R/L$ ) used in the optimization process.

Conventional Design			Agg	ressive	Design			
AR	2.5	3	3.5	4	4	4	4	4
$\Delta R/L$	0.3	0.3	0.3	0.3	0.2	0.4	0.5	0.6

allowed ranges are shown in Table 4. Increased values for  $\lambda_1$  and  $\lambda_2$  were used to allow for a more expressive diffusing duct.

Table 4: Ranges of the optimization variables used in the study.

Variable	Range
$x_{\text{mid}}$	[0.275, 0.725]
$r_{ m mid}$	[0.3, 0.8]
κ, deg	[10, 60]
$\lambda_1$ - $\lambda_2$	[0.05, 0.75]
$\lambda_3$ - $\lambda_8$	[0.05, 0.5]

The goal of the optimization is to minimize the total pressure drop over the duct while maintaining a desired thermal load. Given the inlet temperature of  $13\,^{\circ}\text{C}$  and the water temperature of  $5\,^{\circ}\text{C}$  a target temperature drop of  $10\,^{\circ}\text{C}$  was chosen. This is expected to return a heat-exchanger design that will result in a total pressure drop of roughly  $1\,\%$ , which ensures that the experimental facility can drive the flow at the simulated mass flow. The optimization target,  $f_{target}$ , is therefore to minimize the total pressure drop between the inlet and the outlet,

$$f_{target} = \Delta p_{overall} = \frac{p_{0,inlet} - p_{0,outlet}}{p_{0,inlet}}$$
(14)

where  $p_{inlet}$  and  $p_{outlet}$  is the mass averaged total pressure at the inlet and outlet of the air domain respectively. The stopping criterion for the optimization was defined as 500 iterations. This threshold was chosen to provide a sufficient margin beyond the point of convergence, as all optimization runs consistently identified the best-performing duct within 250 iterations.

# 2.7 Validation cases

The CFD model was verified against two different diffuser geometries. The metric used to validate both ducts was the pressure recovery coefficient,

$$C_{pr} = \frac{p_e - p_t}{p_{0,t} - p_t} \tag{15}$$

and it provides a measure of how much dynamic pressure is converted into static pressure. The subindex e corresponds to the diffuser exit and subindex t corresponds to the throat just ahead of the diffuser. The static pressures are obtained trough area averaging, while the total pressure is calculated through mass flow averaging.

#### 2.7.1 Conical diffuser

Experimental data for conical diffusers with an inlet Mach number of 0.4 and a Reynolds number of 227,000 was obtained from [9]. The diffusers were parametrized by the ratio between the length of the duct and the throat diameter  $L/D_t$ , the area ratio AR, and the blockage ratio  $B_T$ . The geometry consists of an inlet tube which is used to build up a boundary layer to obtain the desired blockage ratio, followed by the diffuser duct and a discharge plenum. The values used match the experimental setup, with the throat diameter being equal to  $D_t = 1.27\,\mathrm{cm}$  and the plenum diameter being equal to 20.3 cm. The studied set of ducts consisted of two blockage ratios, 3% and 12%, two area ratios, 4 and 8, and lengths spanning from L/D = 4 to L/D = 24. An example geometry for  $B_T = 3\%$ , L/D = 8 and AR = 8 is shown in figure 6.

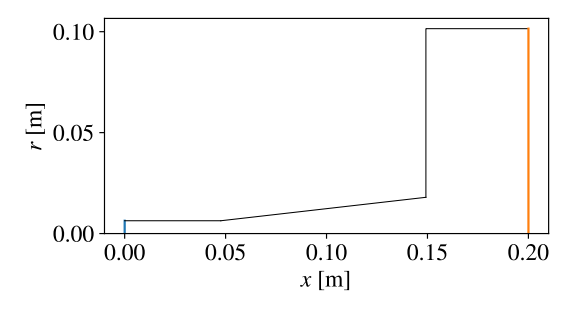


Figure 6: Meridional view of a conical diffuser with AR = 8, L/D = 8 and an inlet length that gives  $B_T = 3\%$ . The diffuser channel starts at x = 0.05 m and ends at x = 0.15 m.

## 2.7.2 Annular diffuser

Experimental data for annular diffusers with an inlet Mach number of 0.2 and a Reynolds number of 600,000 was obtained from [10]. The diffusers consisted of two parallel slanted walls, which due to the axisymmetry diffuses the flow when increasing the mean radius. The geometry used was parametrized through the ratio between the average wall length and the inlet hydraulic diameter  $\bar{L}/D_h$ , the blockage ratio  $B_T$  and the slope of the parallel walls  $\phi$ . The investigated ducts had a blockage ratio of 2%, a slope of 15° and lengths spanning  $\bar{L}/D_h = 2.28$  to  $\bar{L}/D_h = 13.1$ . An example duct with  $\bar{L}/D_h = 5.66$  is shown in Figure 7.

# 3 Results

This section presents and discusses the results from the validation case, the mesh convergence study, the optimization campaign and the isotropic heat exchanger case study.

### 3.1 Validation cases

The two sections below present the results from the validation study, as described in section 2.7.

# 3.1.1 Conical Duct

Figures 8 shows the pressure recovery coefficient  $C_{pr}$  as a function of the ratio between duct length and inlet diameter,

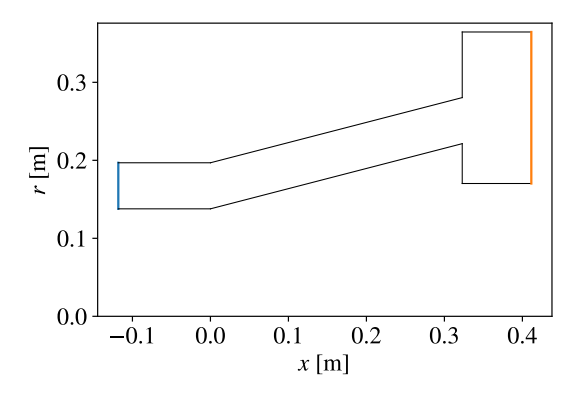
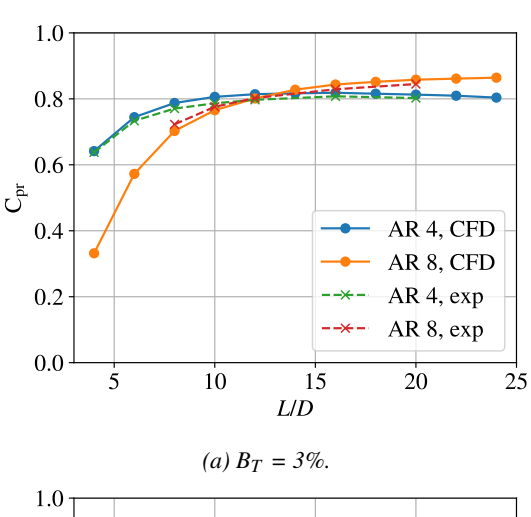


Figure 7: An annular diffuser used for validation with  $\bar{L}/D_h = 5.66$ . The inlet is shown in orange, and the outlet in black. The diffuser channel starts at x = 0.0 m and ends at x = 0.32 m.

for conical diffusers with area ratios of 4 and 8, respectively. The solid lines represent CFD predictions, while the dashed lines correspond to experimental data from [9].



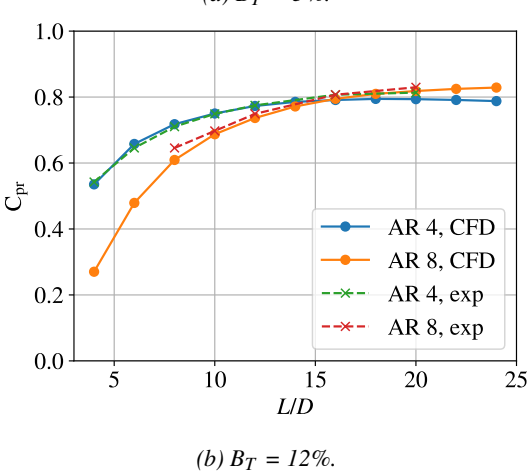


Figure 8: Pressure recovery coefficient against the ratio between duct length and inlet diameter. (a): 3% inlet blockage ratio, (b): 12% inlet blockage ratio.

The results show that the CFD model accurately captures the diffusive behavior of short conical ducts. Notably, the simu-

lations also reproduce the reduction in pressure recovery associated with higher blockage ratios. This increases the trust-worthiness of the results of the optimization campaign as the inlet boundary conditions used produced velocity profiles at the inlet with a blockage ratio of about 24 %.

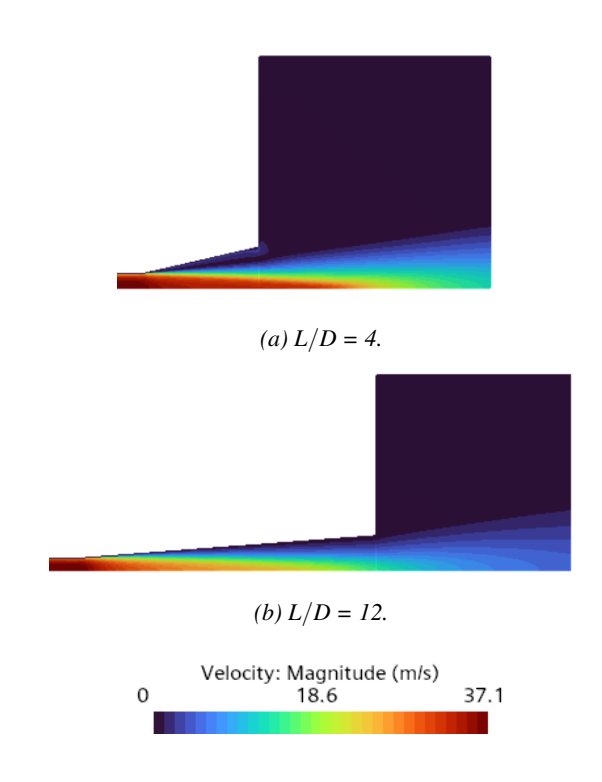


Figure 9: Pressure recovery coefficient against the ratio between duct length and inlet diameter for two ducts with AR = 4 and  $B_T = 12\%$ .

The velocity fields for geometries with AR = 4,  $B_T = 12\%$  and L/D = 4 or L/D = 12 are shown in Figure 9. The short duct shows significant separation, however as the Figure 8 showed the diffusive effects of the ducts are still matching well between the experimental and numerical datasets.

## 3.1.2 Annular duct

Figure 10 present the pressure recovery coefficient  $C_{pr}$  as a function of the ratio between duct length and inlet diameter for the annular diffuser. The solid line is the CFD results while the dashed line is experimental data from [10]. The figures shows an over prediction in the diffusive capacity of the duct.

The annular case was run without an exit plenum, and the outlet was instead placed at the diffuser exit. This was due to unsteady flow behavior in the annular plenum which was not observed in the conical case, due to the stabilizing effect of the axis of symmetry boundary condition. This could be an explanation for why the performance is overestimated, which points to the need of transient methods being needed to accurately estimate the diffusive properties in unsteady flows.

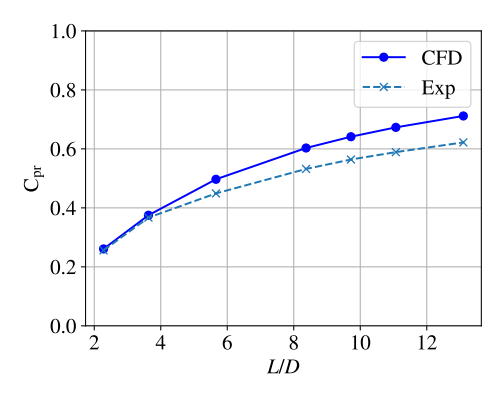


Figure 10: Pressure recovery coefficient against the ratio between duct length and inlet diameter for the annular duct.

## 3.2 Convergence

This section presents the mesh convergence study as well as the solution convergence of the CFD simulations.

### 3.3 Mesh convergence

A mesh convergence study was performed using a representative duct geometry, illustrated in Figure 11, to evaluate the sensitivity of the simulation results to mesh resolution. The mesh size varied from 30,000 to 240,000 cells, and the total pressure drop between the inlet and outlet—normalized by the value obtained using the finest mesh—was used as the convergence metric. The results are presented in Figure 12. Based on the observed trend, the third finest mesh was selected for all subsequent simulations, as it provided an acceptable level of accuracy while substantially reducing computational cost, which was required by the optimization.

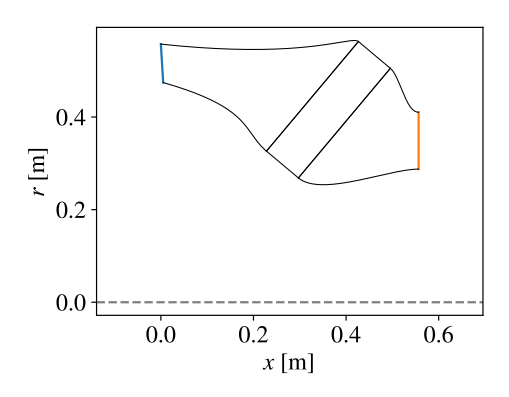


Figure 11: The geometry used in the mesh convergence study.

## 3.3.1 Solution convergence

The convergence of the total pressure drop, here normalized by inlet total pressure, as well as the temperature drop for the AR=4,  $\Delta R/L=0.6$  duct are shown in Figures 13. The sharp increases located at iteration 400 corresponds to when the updating of  $\chi$  is turned on. The convergence histories for all of the optimized designs followed the same trend: a sharp spike at 400 iterations followed by a smooth convergence to a final value with no oscillations observed. The convergence

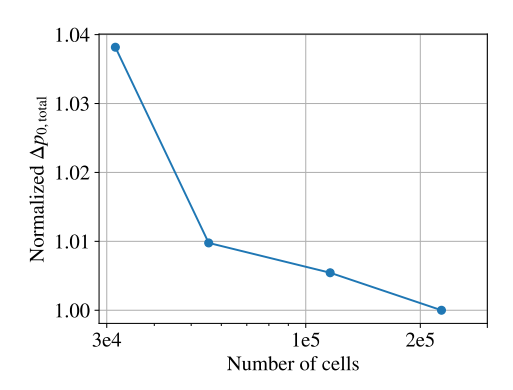
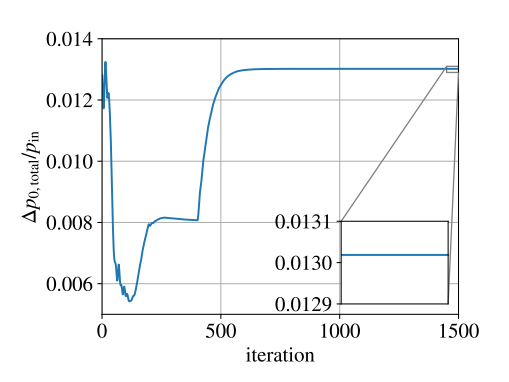


Figure 12: Normalized total pressure drop vs. number of cells in the mesh.

histories from other cases are omitted for brevity due to this similarity.



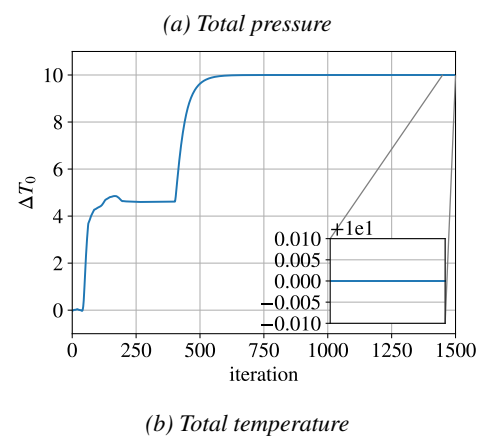


Figure 13: Figures showing the convergence history for the total pressure and temperature drops.

### 3.4 Optimization results

# 3.4.1 Effects of area ratio on performance

The effects of area ratio on performance were investigated by fixing  $\Delta R/L=0.3$  and optimizing the duct to minimize the duct inlet to outlet total pressure drop for different area ratios. This was done for fixed values of area ratios between 2.5 and 4. Figure 14 shows that a larger area ratio gives lower overall losses. As the area ratio increases the HEX entry losses increase while the HEX core losses decrease. The duct losses

are largely negligible in all configurations.

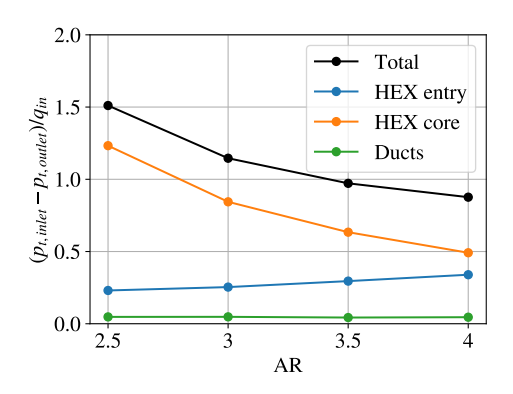


Figure 14: Total, HEX entry, HEX core and duct losses against area ratio for the optimal designs.

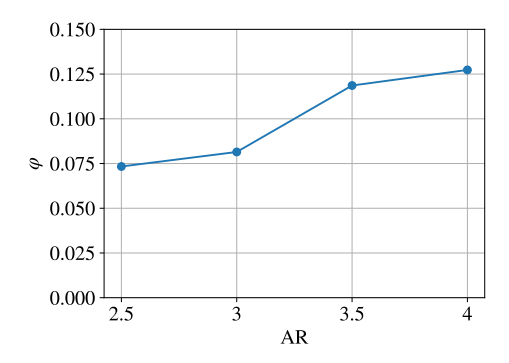


Figure 15: Velocity magnitude non-uniformity at the heat exchanger inlet.

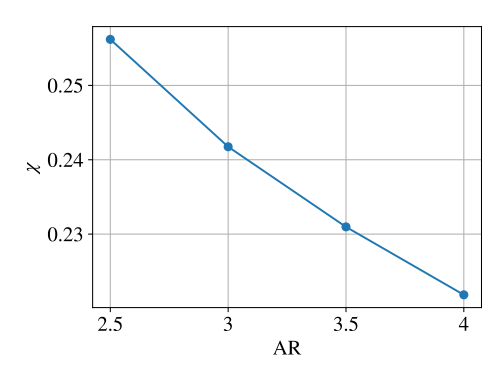


Figure 16: The value of  $\chi$ , which correlates with fin density, against area ratio for the optimal designs.

The increase in HEX entry losses with area ratio is first evident in the rise in non-uniformity, shown in Figure 15, as ducts with larger area ratios are less able to diffuse and turn the flow efficiently. Entry losses are largely caused by the finned structures, which remove velocity in the x'-direction through the large pressure sink term.

The decrease in core losses can be explained through the lowered fin density, as illustrated in Figure 16, and by the reduced velocities through the heat exchanger, seen in Figure 17. A lower fin density results in less friction losses while

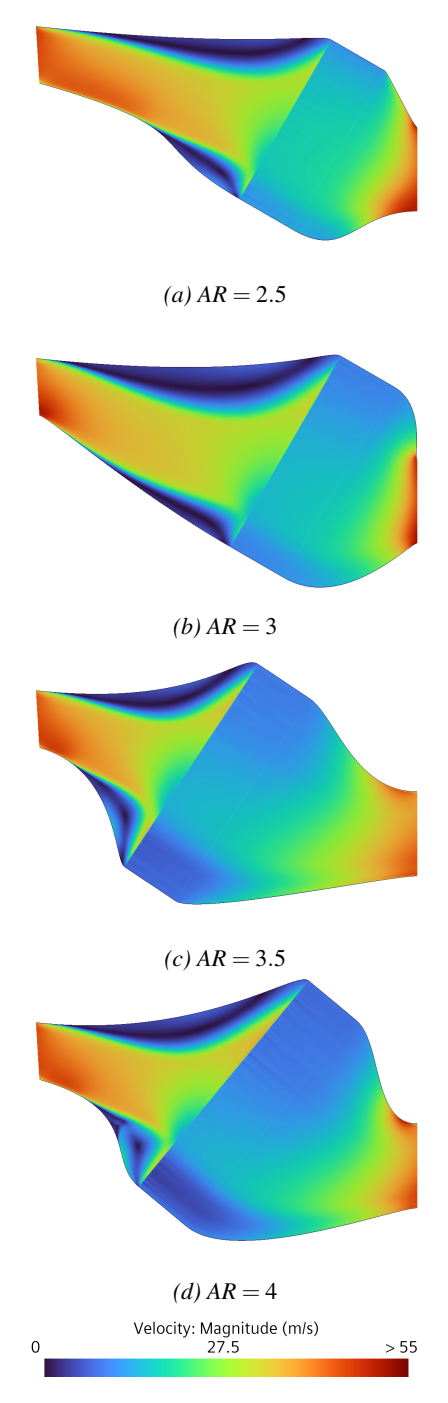


Figure 17: Velocity fields for the four optimized ducts in the area ratio sweep.

lower velocities reduce core losses. This is due to the pressure losses scaling with the square of velocity, whereas heat transfer scales approximately linearly with velocity (Equations 4 and 3).

As the area ratio increases, the duct is less able to diffuse and turn the flow, which increases the entry losses over the HEX. These losses arise because the finned structures effectively removes the velocity in the x'-direction through the large pressure sink term. The effect is accompanied by greater non-uniformity, as illustrated in Figure 15. In addition, lower ve-

locities through the heat exchanger, seen in Figure 17, further reduce the core losses, since pressure losses scale with the velocity squared, whereas heat transfer depends more nearly linearly on velocity (as expressed in Equations 4 and 3).

Observing the velocity fields, Figure 17, shows a clear trend: the optimal design always favors a jet of fluid which impacts the heat exchanger inlet. The jet spreads out across the entire interface which showcases the diffusive capacity of the heat exchanger itself. This is a core finding as previous work expected optimal designs to increase the diffusion by tilting the heat exchanger more relative to the inlet which reduces the effective area of the inlet duct which increases entry losses but also increases velocity magnitude non-uniformity [2].

The total pressure fields presented in Figure 18 shows increased losses in the shorter ducts. These figures also reveal a brighter region in total pressure across the duct near the walls, indicating losses near the walls. At the center of the heat exchanger the flow remains more aligned with the y'-direction which causes the large source term in the x'-direction to not remove as much pressure. This results in a smooth pressure field across the heat exchanger entry. In contrast, near the walls, a significant portion of the velocity is aligned with the x'-direction and the associated dynamic pressure is therefore lost, which accounts for the observed discontinuities.

The total temperature fields, figure 19, shows a uniform temperature decrease in the AR = 2.5 and AR = 3 case, while the larger area ratios show cold spots. These cold spots are due to flow stagnation in the heat exchanger which allows the flow to reach the temperature of the cold side. This behavior indicates that the heat exchanger model is functioning as intended, since a simpler model employing a constant volumetric heat sink would produce unrealistically low temperatures.

### 3.4.2 Effects of duct length on performance

The effects of area ratio on performance are investigated by fixing AR = 4.0 and optimizing the duct to minimize the duct inlet to outlet total pressure drop for different area ratios. This was done for fixed values of  $\Delta R/L$  between 0.2 and 0.6.

Figure 20 show the distribution of losses as the length of the duct decreases. A shorter duct results in increased HEX core losses, as well as increased entry losses for all duct lengths except the shortest configuration. One explanation for this change in loss distribution is that there are different types of configurations with similar performance, making it difficult for a clear trend to emerge as the search space for the optimizer becomes flat. Another explanation for this change in behavior could that the optimization is not fully converged for all the designs. Looking at the HEX core losses in Fig. 20, the fin density in Figure 21 and the velocity uniformity in Figure 22 there is a clear correlation. As the non-uniformity increases the losses increase and a higher fin density is required to meet the required thermal performance. This is due to the pressure drop scaling with the square of the velocity, as discussed in the section above, which causes a less uniform flow through the heat exchanger core to give rise to increased losses. The velocity fields in figure 23 share similar-

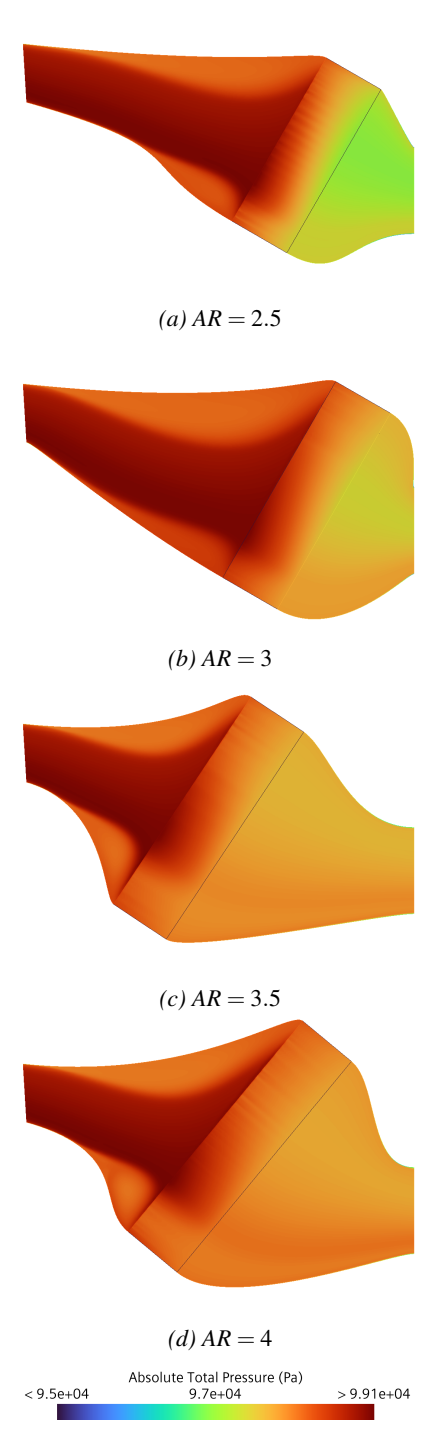


Figure 18: Total pressure fields for the four optimized ducts in the area ratio sweep.

ities to the ducts in the AR-sweep. All designs feature separation regions to some degree. The least aggressive design,  $\Delta R/L=0.2$ , features a partially-attached flow on the hub diffuser wall, similarly to the least aggressive design in the area ratio sweep. As the ducts become very short the separation regions start to diminish as there's simply no space for them to occur. While the shorter ducts do struggle with diffusion, seen through increased non-uniformity, they also struggle to turn the flow which is seen through the increased HEX entry

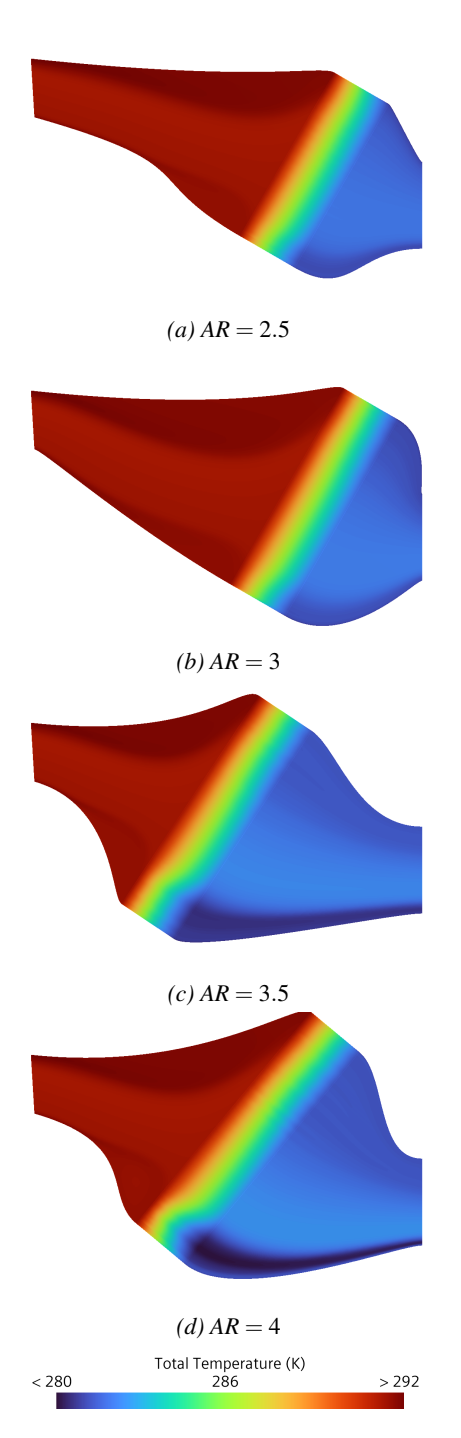


Figure 19: Temperature fields for the four optimized ducts in the area ratio sweep.

losses. Future studies could look to try and use the heat exchanger surfaces themselves as a means to diffuse and turn the flow inside the duct.

The total temperature fields also illustrate how diffusive capacity of the designs decreases as the ducts become shorter. This is seen through the increase of cold spots throughout the heat exchanger. The  $\Delta R/L=0.5$  duct shows a large bulge on the shroud side of the heat exchanger, which gives rise to a large cold spot. The shorter  $\Delta R/L=0.6$  duct is instead moved such that the heat exchanger is more centered relative to the

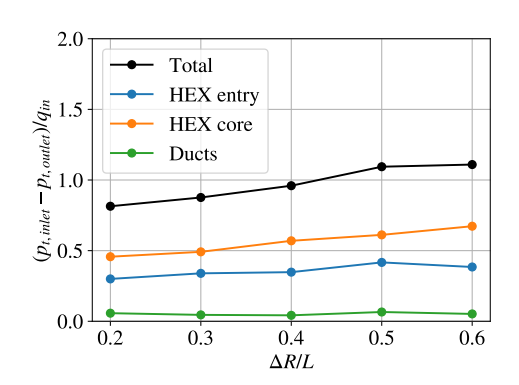


Figure 20: Total, HEX entry, HEX core and duct losses against area ratio for the optimal designs.

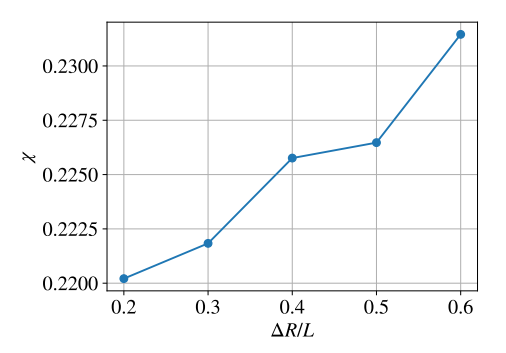


Figure 21: The value of  $\chi$ , which correlates with fin density, against area ratio for the optimal designs.

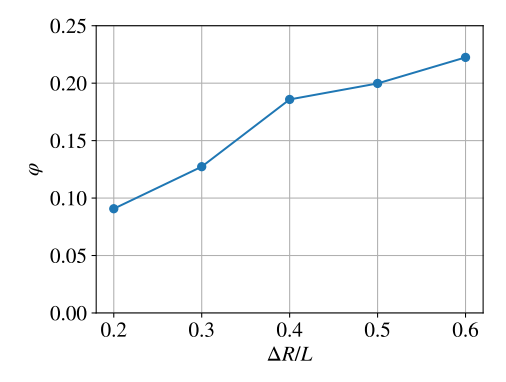


Figure 22: The value HEX inlet-normal velocity uniformity  $\Delta R/L$  for the optimal designs.

incoming fluid jet which instead gives rise to two smaller cold spots, one at the hub and one at the shroud. This could be an indicator that the optimization is not fully converged, but it could also be an indicator that different loss distributions can both be close to optimal when minimizing the total losses.

# 3.5 Isotropic heat exchanger

The  $\Delta R/L=0.3$ , AR=3 duct was chosen to compare the finned heat exchangers with an isotropic one as well as the duct without a heat exchanger. Table 5 presents the losses, non-uniformity and  $\chi$ . Figure 25, show the velocity fields for the three different configurations.

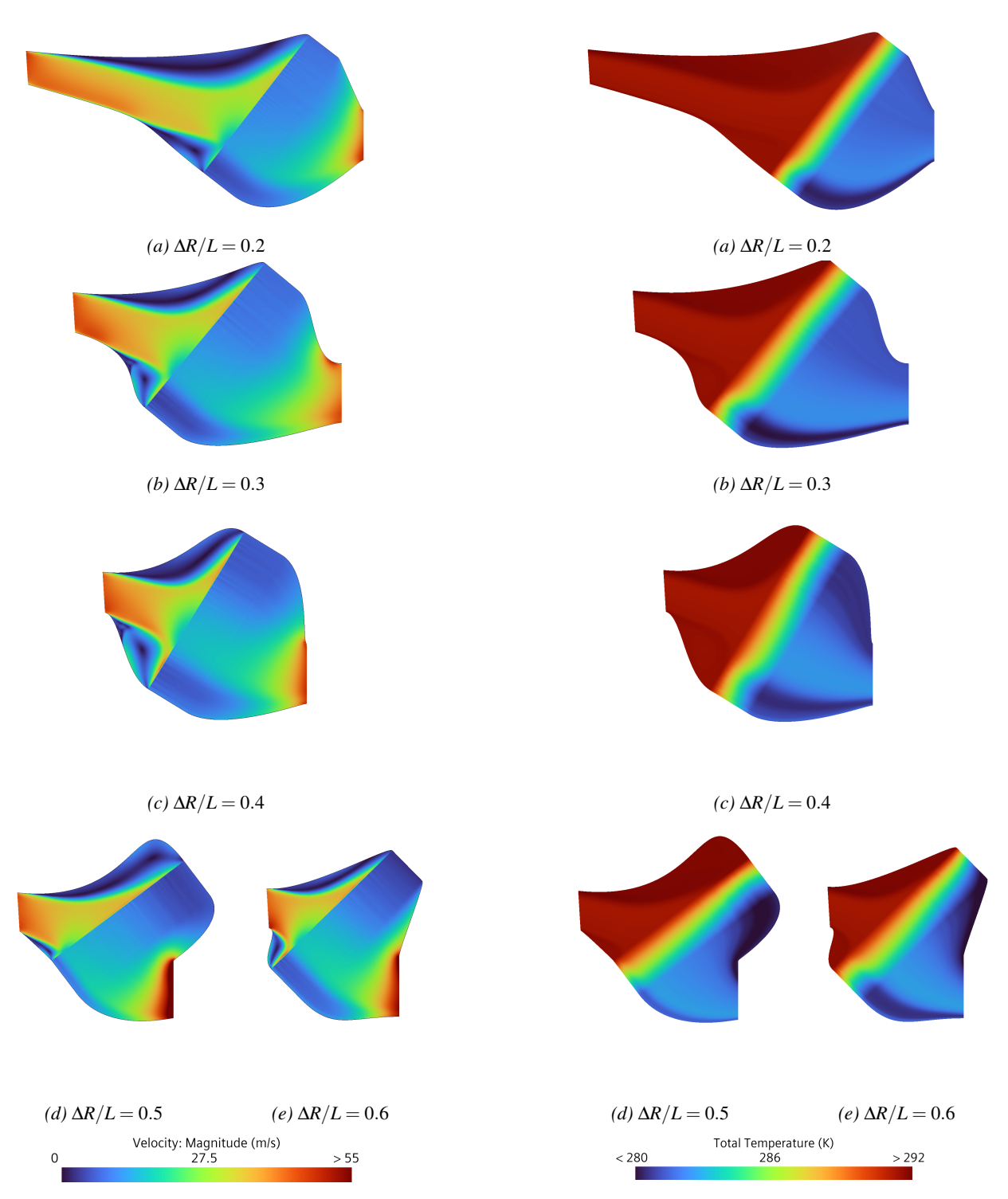


Figure 23: Total pressure fields for the five optimized ducts in the  $\Delta R/L$  sweep.

Figure 24: Total temperature fields for the five optimized ducts in the  $\Delta R/L$  sweep.

The analysis of aerothermal performance presented in Table 5 reveals several notable insights. The pressure losses for the finned and isotropic heat exchanger configurations are nearly identical, differing by about 1 %. In the isotropic case, the reduction in entry losses is traded for higher HEX core losses, for a low net change in performance. This reduction in entry losses arises from the absence of fins, which in the finned

configuration removes a large amount of dynamic pressure. However, the lack of fins also removes the constraint that forces the fluid to follow the shortest possible path through the heat exchanger, along the y'-axis. Consequently, while entrance losses are reduced in the isotropic configuration, they are not entirely eliminated. This is primarily due to the increased freedom of the fluid to traverse significant distances

Table 5: Aerothermal performance for different heat exchanger types

Heat exchanger type	Finned	Isotropic	No HEX
$\Delta T$	10 K	10 K	0 K
$\Delta p_0/q_{ m in}$	1.146	1.159	0.037
$\Delta p_{0, ext{HEX entry}}/q_{ ext{in}}$	0.254	0.143	N/A
$\Delta p_{0, { m HEX~core}}/q_{ m in}$	0.844	0.97	N/A
$\Delta p_{0, ext{ducts}}/q_{ ext{in}}$	0.048	0.046	N/A
Non-uniformity	0.081	0.226	0.565
χ	0.242	0.234	N/A

in the x'-direction within the entry region. Furthermore, the fluid tends to follow a longer trajectory through the core of the heat exchanger, which contributes to higher core losses. This occurs despite the reduction in pressure drop that results from a lower value of  $\chi$ .

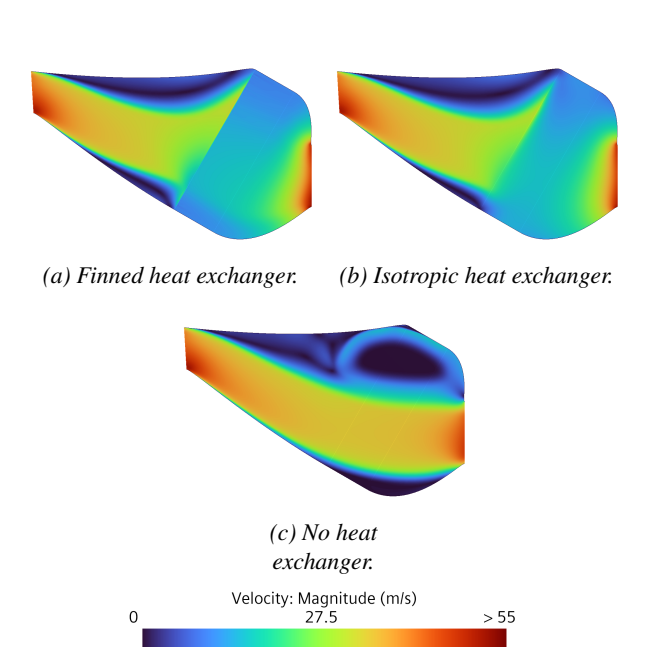


Figure 25: Velocity fields for the optimized  $\Delta R/L = 0.3$ , AR = 3 duct for different styles of heat exchangers.

This difference in flow behavior is further illustrated by the flow field visualizations of the two configurations in Figure 25a and 25b. In the finned heat exchanger, the flow remains aligned with the y'-axis, as the fins restrict lateral diffusion and inhibit mixing. In contrast, the isotropic configuration shows significant mixing inside the heat exchanger which results in a smoother velocity field.

The velocity field for the case without a heat exchanger, Figure 25c, clearly illustrate the diffusive influence of the heat exchangers on the flow behavior. In the absence of a heat exchanger, the flow exhibits the characteristics of a pure jet, with minimal diffusion and a narrow velocity profile confined to the central region of the duct. In contrast, the presence of heat exchangers, both finned and isotropic, promotes greater diffusion, resulting in a broader distribution of the flow across the duct.

## 4 Conclusion

This paper has demonstrated the effectiveness of using coupled models with optimization techniques to conduct rapid design studies. By constraining the designs to achieve the same thermal load the performance comparisons can be simplified and consistency can be ensured across design iterations. This allows for rapid design evaluations, and it's made possible by the embedding of aerothermal performance calculations of heat exchangers directly within the CFD solver.

The conclusions from the parameter sweeps are that higher area ratios and longer ducts reduces aerodynamic losses. Across all configurations, highly separated flow regions were observed, yet the overall level of diffusion remained high. This indicates that the dominant source of diffusion is the heat exchanger itself, rather than the surrounding duct. Although the heat exchanger dominates the diffusion, the large separation regions observed within the ducts may be a consequence of the restrictive geometric parameterization. A more flexible duct parametrization could potentially better adapt to the flow field, mitigating the separation while increasing the pressure recovery in the duct resulting in improved performance.

Additionally, the study found that finned and isotropic heat exchangers yielded similar performance when placed in the same duct geometry. This suggests that the fins are not the primary driver of diffusion. Instead, the dominant mechanism appears to be the velocity-dependent pressure drop induced by the heat exchanger matrix.

Future work could leverage the computational tool developed in the present work to enable new strategies for duct and heat exchanger design. Operating within a continuum framework, the tool supports the evaluation of complex heat exchanger geometries that go beyond simple shapes such as the square diffuser in this work. This flexibility opens up opportunities to explore integrated configurations in which the heat exchanger extends into the duct's diffusing section, varying fin angles throughout the geometry and non-uniform heat exchanger geometries. Such designs have the potential to more effectively redistribute aerodynamic diffusion between the duct and heat exchanger, potentially yielding beneficial synergies through reduced flow separation and improved flow control.

### Acknowledgments

This research work was funded by the Swedish National Aviation Engineering Research Program, NFFP, supported by the Swedish Armed Forces, the Swedish Defense Materiel Administration, Swedish Governmental Agency for Innovation Systems (VINNOVA) and GKN Aerospace.

## References

- [1] European Commission. Flightpath 2050 europe's vision for aviation. Technical report, European Commission, Brussels, December 2011.
- [2] Alexandre Capitao Patrao, Isak Jonsson, Carlos Xisto, Anders Lundbladh, and Tomas Grönstedt. Compact heat

- exchangers for hydrogen-fueled aero engine intercooling and recuperation. *Applied Thermal Engineering*, 243:122538, April 2024.
- [3] Alexandre Capitao Patrao, Isak Jonsson, and Carlos Xisto. Compact heat exchangers with curved fins for hydrogen turbofan intercooling. *Journal of Engineering* for Gas Turbines and Power, 146(11), July 2024.
- [4] William M Kays and A L London. *Compact Heat Exchangers*. McGraw-Hill Companies, 2 edition, October 1964.
- [5] Petter Miltén, Isak Johnsson, Anders Lundbladh, and Carlos Xisto. Generalized method for the conceptual design of compact heat exchangers. *Journal of Engineering for Gas Turbines and Power*, 146(11), August 2024.
- [6] Petter Miltén. Conceptual design of the hydrogenenhanced intercooler. Licentiate Thesis. Chalmers University of Technology, 2024.
- [7] Isak Jonsson, Carlos Xisto, Marcus Lejon, Anders Dahl, and Tomas Grönstedt. Design and pre-test evaluation of a low-pressure compressor test facility for cryogenic hydrogen fuel integration. In *Volume 2A: Turbomachinery Axial Flow Fan and Compressor Aerodynamics*, GT2021. American Society of Mechanical Engineers, June 2021.
- [8] Saleh Rezaeiravesh. BO-GP. https://github.com/ KTH-Nek5000/B0\_GP, 12 2022. Accessed 2025-05-06.
- [9] F. X. Dolan and Jr. Runstadler, P. W. Pressure recovery performance of conical diffusers at high subsonic mach numbers. Contractor Report NASA-CR-2299, NASA, Washington, D.C., July 1973. TN-165.
- [10] G. Sovran and E. D. Klomp. Experimentally determined optimum geometries for rectilinear diffusers with rectangular, conical or annular cross-section. In G. Sovran, editor, *Fluid Mechanics of Internal Flow*, pages 270– 319. Elsevier Publishing Co., Amsterdam, 1967.